Evaluating Fiber Tract Bundling

Eric Begue

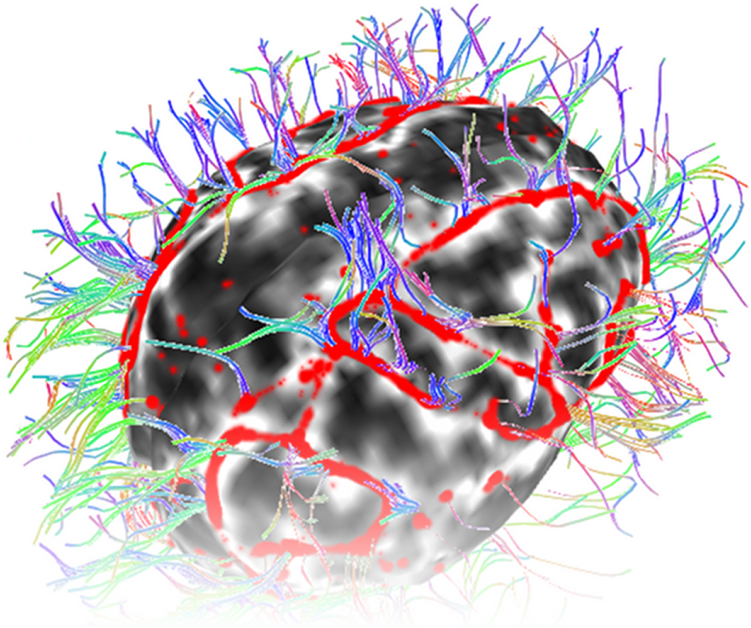

Master Thesis

Supervisors:
Dr. H. Bekker
Dr M.H.F. Wilkinson

December 16, 2011

Evaluating Fiber Tract Bundling

Eric Begue

December 16, 2011

Contents

In Diffusion Tensor Imaging (DTI) a large set of dense fiber tracts representing white matter is generated. Fiber Tract Bundling (FTB) is an experimental technique to bundle tracts. In this way a scalable abstraction is created. This technique displaces the tracts in space and therefore the bundled tracts lose coherence with the anatomy. This loss of information is studied in this work.

In order to investigate how FTB behaves with respect to the anatomy, we developed and implemented an evaluation method that enables the user to monitor the bundling process on a curved surface. The fiber tract bundling is visualized against the Fractional Anisotropy (FA) image, which is used as an anatomical reference.

We present the FTB technique, demonstrate our evaluation method and show the results we have obtained.

Acknowledgements

I would like to thank my supervisors Dr M.H.F. Wilkinson and Dr. H. Bekker, with who discussions was inspiring, and M. H. Everts for his sharing about tracktography.

Chapter 1

Introduction

MRI gives the possibility to visualize internal organs and structure of the human body. Tractography is a specialized MRI technique that allows the visualization of fibrous structure such as muscle or brain white matter. The fiber tracts are computed by a tracking algorithm and displayed as three-dimensional curves. The large number of those curves makes their visualization difficult on a computer screen because of occlusion. To avoid occlusion, tractograpy software usually implements simple techniques such as discarding tracts according to criteria or selecting fiber tracts by mean of Region of Interest (ROI). Fiber Track Bundling (FTB) is a technique with a novel approach to decrease occlusion by producing scalable abstraction of fiber tracts. FTB produces the abstration by changing the geometry of the tracts, which results into a loss of information compared to the original tracts. In this project, we study this loss of information by means of a visualization tool that we developped. We use this tool to investigate how reliable FTB is in term of location, shape and topology.

1.1 Thesis Structure

Chapter 2 provides a comprehensive walk-through about MRI and moreover about how MRI images are produced and what information they contain.

Chapter 3 presents the occlusion problem and the common techniques to used to decrease it. Fiber Track Bundling is introduced as a novel approach to decrease occlusion.

Chapter 4 detailed the FTB algorithm.

Chapter 5 states our research question.

Chapter 6 presents the tool we developed that allows us to visually investigate to behavior of FTB.

Chapter 7 presents the result we obtained.

Chapter 8 presents the conclusions.

Chapter 2

MRI, from NMR to Tractography

In this chapter, we give background information about the Magnetic Resonance Imaging (MRI) technique and about the place of tractography. First, we describe the physical principle that makes MRI possible, that is, Nulcear Magnetic Resonance(NMR). Then, we describe the water diffusion principle and how it is measured with Diffusion Weighted Imaging (DWI). After that, we explain the process of how Diffusion Tensor Imaging (DTI) data are computed from DWI data. Finally, we present the tractography algorithms that produce three-dimensional curves representing fiber tracts from DTI data.

2.1 Magnetic Resonance Imaging

Magnetic Resonance Imaging (MRI) is a technique that allows detailed visualization of internal organs of the human body. MRI is nowadays widely used in medical applications.

MRI exploits an interesting magnetic property of hydrogen atoms. In 1946, Bloch and Purcell, improving the work of Isidor Rabi [RZMK38], observed that hydrogen nuclei emit a radio signal when they are placed in a strong magnetic field and are exposed to a radio signal emitted at an appropriate frequency [Blo46]. This phenomenon is called Nuclear Magnetic Resonance (NMR), and it is more detailed in Section 2.1.1.

MRI is also known as Nuclear Magnetic Resonance Imaging (NMRI). The original terminology was avoided, because it contains the word -nuclear [Gol07]. That word (which reminds of nuclear weapons) makes patients, not acquainted with particle physics, a bit anxious when invited to be scanned.

The NMR effect, as a result, makes hydrogen nuclei to emit photons. This emission produces a radio signal that is detected by a sensor in the MRI scanner. This signal is used to infer the three-dimensional position of the nuclei.With the nucleus three-dimensional position determined, a volumetric image representing

the scanned body part is constructed. There are several types of MRI images, also called weightings, which means that MRI images do not always encode the same type of information.

In 1971, Raymond Damadian build the first MRI scanner and used it as a mean to detect tumors [Dam71]. This achievement was the first medical application of MRI.

In the human body, hydrogen can be found in various tissue types such as skin, fat, muscle or other. The molecular and cellular organization characterizes the tissue type and may respond with a specific signal. It is possible to discriminate between the tissue types by controlling the NMR setting.

2.1.1 Nuclear Magnetic Resonance (NMR)

If we can create an image of the body or a part of it, it implies that the body emits a signal that is detected by the scanner. In this chapter we describe the phenomenon and the techniques involved in the generation of that signal.

PROTON MAGNETIC MOMENT

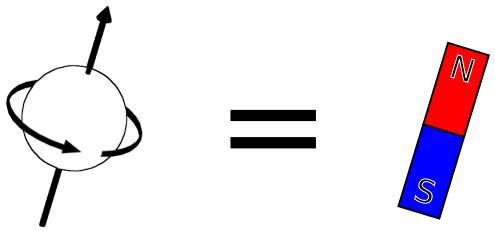

Figure 2.1. Analogy of a nucleus as a tiny magnet bar.

A proton, a nucleus also known as hydrogen ion H^+, is a positively charged particle and has a spin, that is, an angular momentum that makes it rotate about its own axis. From electromagnetism, we know that any moving charge generates a magnetic field. Therefore, because of its spin, a proton has a magnetic moment $\vec{\mu}$, which is a vector oriented from the south to the north pole, characterizing its magnetic field. The magnetic moment $\vec{\mu}$ is directly proportional to the angular momentum $\vec{J}$:

$$\vec{\mu} = \gamma \vec{J}, \tag{2.1}$$

where γ is the gyromagnetic ratio and it is specific to the nucleus type.

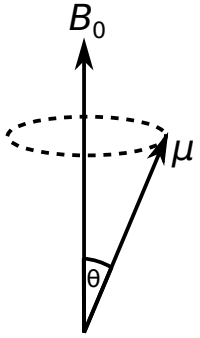

Figure 2.2. Precession of the magnetic moment $\vec{\mu}$ around the magnetic field $\vec{B_0}$

A nucleus can be conceived as a tiny magnet bar, as illustrated in Figure 2.1. When it is placed in a strong (e.g. 1.5 T) magnetic field $\vec{B_0}$ it undergoes a torque. This turning force makes $\vec{\mu}$ to be aligned with $\vec{B_0}$, in the same way a compass needle is getting turned by a nearby magnet. However this analogy is not to be taken too far. Because of a quantum mechanic behavior, the magnetic moment $\vec{\mu}$ is not completely aligned with $\vec{B_0}$, that is, there is a non-zero angle θ between them. Because of this constraint and the influences of $\vec{J}$ and $\vec{B_0}$, the magnetic moment $\vec{\mu}$ precesses around the axis in the direction of $\vec{B_0}$, as shown in Figure 2.2. This precessing movement is described with the equation:

MAGNETIC TORQUE

MAGNETIC MOMENT PRECESSION

$$\frac{d\vec{J}}{dt} = \vec{\mu} \times \vec{B_0} = \gamma \vec{J} \times \vec{B_0} = \gamma J B_0 \sin\theta \vec{n}, \tag{2.2}$$

where the symbol $\times$ denotes the vectorial cross product and $\vec{n}$ is the unit normal vector perpendicular to both $\vec{J}$ and $\vec{B_0}$.

By deriving the precession frequency $\vec{\omega_0}$ from this equation (not shown here), it is found that:

$$\vec{\omega_0} = \pm\gamma\vec{B_0}. \tag{2.3}$$

LARMOR EQUATION

This equation is known as the Larmor equation, which states that the precessional frequency $\vec{\omega_0}$ of a nucleus is proportional to the static magnetic field $\vec{B_0}$.

There is a second quantum behavior to be noted here, which explains the plus-minus sign ($\pm$) in Equation (2.3). When the nucleus is exposed to a static magnetic field $\vec{B_0}$, it precesses in either two orientations, spin-up or spin-down. When the nucleus is in the spin-up or parallel state, its magnetic moment $\vec{\mu}$ is almost aligned in the direction of the static magnetic field $\vec{B_0}$, while in the spin-down state or anti-parallel state, $\vec{\mu}$ is oriented in the opposite direction of $\vec{B_0}$. The proton "chooses" one of thoses states depending on the energy it has. The spin-down state requires more energy than the spin-up state.

SPIN-UP/DOWN

In either state, the proton is stable, so it precesses persistently in its chosen state. However the spin can be flipped (spinning in the opposite direction), by gaining or loosing a specific amount of energy as electromagnetic wave or photon. A proton in the low energy state pulsed by electromagnetic wave at a certain frequency will absorb a photon and it is promoted to the high-energy

SPIN FLIPPING

state. When a proton is in the high energy state, because of the interaction with the environment, it can emit the absorbed energy as a photon, and turn into the low-energy state.

PHOTON ABSORPTION/EMISSION

When a proton is in the spin-up state (low energy state), it's has been found that the RF field frequency necessary to flip its spin-down (high energy state), the resonance frequency, is exactly the Larmor frequency:

RESONANCE FREQUENCY

$$\omega_0 = \gamma B_0. \tag{2.4}$$

So far, we have described the behavior of the proton at the atomic scale. At this point, we are leaving the microscopic level and zoom out to a macroscopic level, by considering the NMR effect within a small volume containing a large number of protons.

When considering a large number of nuclei, the ratio of spin-up and spin-down protons is given by the Boltzman equation:

BOLTZMAN EQUATION

$$\frac{N_{\text{up}}}{N_{\text{down}}} = \exp(\frac{\gamma \frac{h}{2\pi} B_0}{kT}), \tag{2.5}$$

where h is the Plank's constant, k is the Boltzman's constant and T is the temperature. At the normal body temperature (37 °C) and in a field of 1.5 T, $\frac{N_{up}}{N_{down}} = 1.000004$, which means that for every million spin-down protons, there are a million-and-four spin-up protons. It is this very small difference that allows an MRI scanner to measure a signal.

Let's say we have N protons within a small volume. When we expose this sample to a static magnetic field $\vec{B_0}$, each proton's magnetic moment precesses according to Equation (2.2). At a given time, the net magnetization is:

NET MAGNETIZATION

$$\vec{M_0} = \sum_{i=1}^{N} \vec{\mu_i}. \tag{2.6}$$

The magnetic moments precess out of phase with each other, that is, the their phase are randomly distributed. As a net effect, the net magnetization $\vec{M_0}$ is aligned with the static magnetic field $\vec{B_0}$. Furthermore, since there are more spin-up protons, the orientation of $\vec{M_0}$ is in the same direction of $\vec{B_0}$. We can conclude that the net magnetization $\vec{M_0}$ of a sample exists because of the tiny differences in the number of spin-up and spin-down protons and it is aligned with the static field $\vec{B_0}$ at equilibrium.

The net magnetization $\vec{M_0}$ is very small compared with the strong static field $\vec{B_0}$. The magnitude of $\vec{B_0}$ is in order of tesla (T) and the magnitude of $\vec{B_0}$ is in order of microtesla (μT).

In the equilibrium condition it is not possible to measure $\vec{M_0}$. The measurement of $\vec{M_0}$ is possible with a sensor (a coil) that is sensible only to magnetization in the transversal plane, which is the plane perpendicular to $\vec{B_0}$. When $\vec{M_0}$ is at equilibrium, its projection into the transversal plane is null, thus not measurable. Therefore we need to push $\vec{M_0}$ away from B_0, which is achieved by using a radiofrequency field $\vec{B_1}$.

MEASURING $\vec{M_0}$

When the radiofrequency field $\vec{B_1}$ is activated, $\vec{M_0}$ moves away in a precessional movement from $\vec{B_0}$. The trajectory of the tip of $\vec{M_0}$ describes a spiral around $\vec{B_0}$ at a rotational speed equal to the Larmor frequency, and the radius of that spiral increases as $\vec{M_0}$ moves away from with $\vec{B_0}$. This precession of $\vec{M_0}$ generates a rotating magnetic field in the transversal plane which generates a signal in the transversal coil. It is that signal that Bloch and Purcell observed and described by the Bloch equations in 1946 [Blo46]. This signal is called the Free Induction Decay signal and it is further described in Section 2.1.3.

The Bloch equations is a mathematical model that describes the movement of the net magnetization $\vec{M_0}$ in the presence of the static magnetic field $\vec{B_0}$ and the radiofrequency field $\vec{B_1}$. Those equations are detailed in the Section 2.1.2.

BLOCH EQUATIONS

Summarizing, NMR is composed of three phases:

1. **Magnetic Moment orientation** The magnetic moments of the nuclei are oriented using a strong magnetic field. A single nucleus can be conceive as a small magnet bar, which can be oriented by using a bigger magnet, in the same way a compass needle is oriented by a nearby magnet.

2. **RF Pulse** A radio emitter is turned on very briefly in order to pulse an electromagnetic field at specific frequency (the Larmor frequency), which causes the nuclei to flip their spin (spin in the opposite orientation) and being in an a higher energy state because each neuclei has absorbed one photon. This pulse field is oriented so it is perpendicular to the magnetic field in order to increase the strength of the signal emitted by the nucleus.

3. **Relaxation** When the RF pulse stops, the nuclei return from a high-energy state to a low-energy state, releasing the stored energy as a photons. This releasing of photons is a radio signal absorbed and converted to an electric signal. Also, as the nucleus is no more influenced by the magnetic field, it progressively loose its alignment. This alignment decay is measured as two components: T_1 and T_2 (see Figure 2.4).

2.1.2 The Bloch Equations

Bloch and Purcell described the NMR phenomenon with a set of equations [Blo46]. Those equations model the NMR effect at a macroscopic scale; they do not describe NMR at the atomic level. In other words they are phenomenological equations, that is, they are based on empirical observation.

The Bloch equations in laboratory (stationary) frame of reference are:

BLOCH EQUATIONS COMPONENTWIZE FORM

$$\begin{array}{l} \frac{dM_x}{dt} = \gamma(\vec{M} \times \vec{B})_x - \frac{M_x}{T_2} \\ \frac{dM_y}{dt} = \gamma(\vec{M} \times \vec{B})_y - \frac{M_y}{T_2} \\ \frac{dM_z}{dt} = \gamma(\vec{M} \times \vec{B})_z - \frac{M_z - M_0}{T_1} \end{array} , \tag{2.7}$$

where:

- $\vec{M}$ is the net nuclear magnetization of the sample.

- $\vec{B}$ is the magnetic field, which include both $\vec{B_0}$ and $\vec{B_1}$.
- γ is the gyromagnetic ratio.
- T_1 and T_2 are the relaxation times (detailed in Section 2.1.5).
- M_0 is the magnitude of the net nuclear magnetization at equilibrium (that is aligned with $\vec{B_0}$).
- $\vec{M} \times \vec{B}$ is the cross product of those vectors.

$\vec{M}$ and $\vec{B}$ are time dependent. They should be formally written $\vec{M}(t)$ and $\vec{B}(t)$. This notation is avoided for readability.

BLOCH EQUATIONS VECTORIAL FORM

The equations can be rewritten in a vectorial form:

$$\frac{d\vec{M}}{dt} = \gamma(\vec{M} \times \vec{B}) - \begin{pmatrix} \frac{M_x}{T_2} \\ \frac{M_y}{T_2} \\ \frac{M_z - M_0}{T_1} \end{pmatrix}. \tag{2.8}$$

The vectorial forms (2.8) is a more condensed form of the componentwize form (2.7) and it highlights two terms; the torque and the relaxation. The torque term $\gamma(\vec{M} \times \vec{B})$ is a force that pushes $\vec{M}$ away from the z-axis and makes it to precess. The relaxation term $-(\frac{M_x}{T_2}, \frac{M_y}{T_2}, \frac{M_z - M_0}{T_1})^T$ is a kind of damping force that pulls $\vec{M}$ toward the z-axis so that it returns to equilibrium. The smaller the relaxations times T_1 and T_2 are, the quicker $\vec{M_0}$ returns to equilibrium.

$\vec{B_0}$- z-AXIS CONVENTION

The vector $\vec{B}$ is composed of two components, the strong static magnetic field $\vec{B_0}$ and the transversal radiofrequency field $\vec{B_1}$, $\vec{B} = \vec{B_0} + \vec{B_1}$. By convention, the z-axis of the laboratory stationary frame of reference is aligned with $\vec{B_0}$, therefore the x and y components of $\vec{B_0}$ are null and its z component is its magnitude, $\vec{B_0} = (0, 0, B_0)^T$. The radiofrequency field $\vec{B_1}$ is a magnetic field that rotates in the transversal plane perpendicular to $\vec{B_0}$, that is, the xy-plane. The radiofrequency field $\vec{B_1}$ is given by:

RADIOFREQUENCY FIELD DEFINITION

$$\vec{B_1} = \begin{pmatrix} B_1 \cos \omega t \\ B_1 \sin \omega t \\ 0 \end{pmatrix}, \tag{2.9}$$

where ω is the is the angular frequency, which is equivalent to the Larmor frequency.

For educational purpose, a simulator that demonstrates the dynamics of NMR is available on the Internet at:

`http://www.drcmr.dk/bloch`

2.1.3 Free Induction Decay Signal

When the radiofrequency field $\vec{B_1}$ is pulsed, the net magnetization $\vec{M}$ is no more aligned with the z-axis. That angle between $\vec{M}$ and the z-axis is a function of the strength and duration of $\vec{B_1}$ pulse. There are two pulse types commonly used during an MRI scanning, the 90° pulse and the 180° pulse. Those two pulses bring the net magnetization $\vec{B_0}$ at an angle of 90° and 180° respectively from the z-axis. They are used to produce a phenomenon known as Spin-Echo (see Section 2.1.4).

When the radiofrequency field $\vec{B_1}$ is turned off, a signal in the transversal plane can be measured, whose strength is proportional to the length of the projection of $\vec{M}$ on the xy-plane. As the net magnetization $\vec{M}$ goes to equilibrium by aligning again with the z-axis, that signal decreases in intensity. This signal is known as the Free Induction Decay (FID). FID SIGNAL

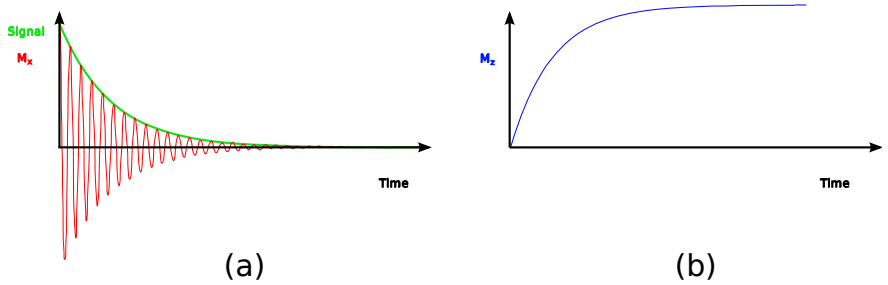

Figure 2.3. (a) The shape of the x-component of $\vec{M}$, the Free Induction Decay signal and (b) the z-component of $\vec{M}$ after a 90° radiofrequency pulse $\vec{B_1}$.

Figure 2.3 shows the form of the x-component of $\vec{M}$ and the corresponding FID signal just after the 90° radiofrequency pulse is switched off, as well as the z-component of $\vec{M}$. As $\vec{M}$ returns to equilibrium, the FID signal decay exponentially while M_z recover exponentially.

2.1.4 Spin-Echo

In Section 2.1.3, we have seen that the net magnetization $\vec{M}$ can be moved from the z-axis using a radiofrequency pulse $\vec{B_1}$ and that the angle between $\vec{M}$ and the z-axis is function of the duration and the strength of that pulse. In this section, we describe what the Spin-Echo phenomena is and how it is produced by using the radiofrequency pulse $\vec{B_1}$.

An MRI scanner can produce a radiofrequency pulse $\vec{B_1}$ that brings the net magnetization $\vec{M}$ at a desired angle from the z-axis. There are two specific angles, 90° and 180°, used to produce the Spin-Echo effect. The pulses producing those angles are simply called the 90°-pulse and the 180°-pulse.

The Spin-Echo is based on the precession dephasing of the nuclei. A nucleus interacts with the static magnetic field but also interacts with its local environment, in which there are other nuclei producing their own tiny magnetic field. So, the momentum of a nucleus is function of the atomic configuration

of its environment. Therefore, the nuclei within a sample composed of different molecules do not precess at the same speed. As a consequence, their precession phase changes dynamically relatively to each other. This dephasing explains the decaying of the FID signal (see Section 2.1.5).

When the net magnetization $\vec{M}$ is at equilibrium, that is, aligned with the static magnetic field $\vec{B_0}$, the nuclei are spinning out of phase. The first step in the creation of the Spin-Echo is to produce a 90°-pulse, which makes the nuclei to precess in phase. Right after this pulse, the net magnetization $\vec{M}$ is rotating perfectly in the xy-plane, which makes the FID signal to be at its maximum. But, as the time passes, this signal progressively decay because of the dephasing of the nuclei. The second step is to produce a 180°-pulse, which inverts the angular momentum of each nucleus. This angular momentum inversion, as an effect, makes the nuclei to precess in the opposite direction or backward. This backward motion makes the neuclei to re-phase again. During the re-phasing of the nuclei, the FID signal increases producing an echo, hence the name of the phenomena. After some time, the nuclei are in phase just as they were just after the 90°-pulse, the FID signal reaches a peak again, before decreasing as the nuclei dephase again.

2.1.5 Relaxations Times: T_1 and T_2

In Section 2.1.2, we have seen that the net magnetization $\vec{M_0}$ is aligned with the static magnetic field $\vec{B_0}$ at equilibrium and that $\vec{M}$ spirals around the z-axis when pulsed by a radiofrequency field $\vec{B_1}$, producing a signal in the transversal xy-plane. Also we have seen that the signal decays as $\vec{M_0}$ returns to equilibrium and the decaying speed is given by T_1 and T_2 (see Equation 2.8). In this section, we are going to have a closer look at the underlying phenomena and their use to produce weighted images.

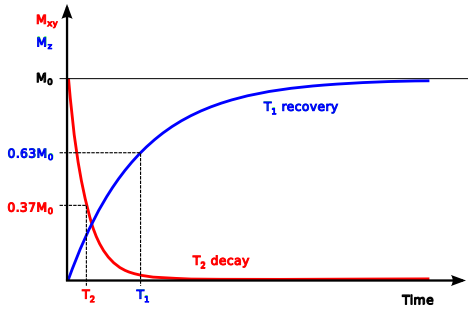

Figure 2.4. Shape of relaxation components T_1 recovery and T_2 decay.

T_1 is the elapsed time for the z-component of the net magnetization M_z to recover 63% of M_0 after the radiofrequency $\vec{B_1}$ pulse. T_2 is the time for the FID signal to drop down to 37% of M_0. Figure 2.4 shows the shape of the T_1 recovery and the T_2 decays. The duration of T_1 is much longer that T_2.

In 1948, Bloembergen, Purcell and Pound explained the relaxation of the net magnetization $\vec{M}$ by molecular dynamic [BPP48]. This work is known as BPP Theory

the BPP Theory.

After the radiofrequency pulse, the protons return to their equilibrium orientation because of the interaction with their environment, which makes the net magnetization $\vec{M}$ to re-align with the static magnetic field $\vec{B}_0$. The interactions are of two types, the spin-lattice (T_1 recovery) and spin-spin (T_2 decay).

The spin-lattice (proton-$\vec{B}_0$) relaxation (T_1) is the increasing of the z-component of $\vec{M}$. This recovery is caused by the release of energy by the spin-down protons, which flip their spin up, and therefore contribute to the net magnetization in the direction of $\vec{B}_0$. The protons release their energy randomly until the ratio of spin-up to spin-down protons reaches equilibrium (see Equation 2.5). T_1 RECOVERY

The spin-spin (proton-proton) relaxation (T_2) is the decay of the xz-component of the $\vec{M}$. This decay is caused by dephasing of the precessing protons. The proton magnetic moment is influenced by the magnetic field in the environment, which includes the magnetic field of the protons in the neighborhood. T_2 DECAY

Both T_1 and T_2 depend and the molecular configuration of the sample. That is, the values of those relaxation times is function of the tissue type. Therefore they can be used to discriminate tissue types. For example, when scanning the human brain with 1.5 T scanner, the white matter has $T_1 = 560$ ms and $T_2 = 82$ ms, while the grey matter has $T_1 = 1000$ ms and $T_2 = 92$ ms [SZZS01].

2.2 Diffusion Weighted Imaging

In liquid water, due to thermal motion, the molecules are constantly in movement and are bouncing with each other. This makes the trajectory of individual water molecule being random. This movement is a Brownian motion.

When there is no microscopic physical constraint, water diffusion is isotropic. For example, in a glass of water, the molecules diffuse in any direction with the same probability. In that case, the diffusion can be characterized by a single scalar, the diffusion coefficient D. ISOTROPIC DIFFUSION

But in the body the water diffusion is constrained by the biological environment. In fibrous tissue (e.g. muscle or brain white matter) the diffusion is anisotropic [LBBL$^+$88] [LBTMP91] [Tan79]. That is, the spread of the water molecule is not the same in every direction. Therefore, a single diffusion D coefficient is not enough to characterize the diffusion. This coefficient D would rather be a function of direction. Actually, the diffusion in 3-dimension is best described by the diffusion tensor, which is a 3-by-3 matrix: ANISOTROPIC DIFFUSION DIFFUSION TENSOR

$$\mathbf{D} = \begin{pmatrix} D_{xx} & D_{xy} & D_{xz} \\ D_{yx} & D_{yy} & D_{yz} \\ D_{zx} & D_{zy} & D_{zz} \end{pmatrix}. \tag{2.10}$$

The multiplication of $\mathbf{D}$ by a vector $\vec{e}$ is a vector which as the same direction of $\vec{e}$ but a different length or scale λ: EIGEN VALUE/VECTOR

$$\mathbf{D}\vec{e} = \lambda\vec{e}, \tag{2.11}$$

where $\vec{e}$ is called an eigenvector and λ is its corresponding eigen value.

It is possible to compute the principal diffusion direction from the eigen value and eigenvector algebra. Diagonalization of the diffusion tensor $\mathbf{D}$ provides the three eigenvectors ($\vec{e_1}$, $\vec{e_2}$, $\vec{e_3}$) and the their three corresponding eigen values (λ_1, λ_2, λ_3). For the three eigen values, it holds that $\lambda_1 > \lambda_2 > \lambda_3$ in the general case.

The diffusion tensor $\mathbf{D}$ can be visualized as an ellipsoid (Figure 2.5), whose principal directions represent the directions in which the diffusion is fastest. To draw such ellipsoid, one can multiply $\mathbf{D}$ with a vector $\vec{e}$ with different orientations but same length. The tips of the resulting vectors are points on the surface of the ellipsoid. The main directions (e.i. major, medium, and minor) of the diffusion ellipsoid correspond to the eigenvectors $\vec{e_1}$, $\vec{e_2}$ and $\vec{e_3}$ respectively.

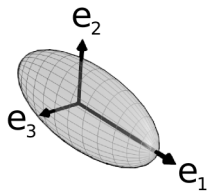

Figure 2.5. Visualization of the diffusion tensor as an ellipsoid, whose principal directions are the vectors $\vec{e_i}$.

The signal intensity S measured after a spin echo sequence is:

$$S = S_0 \exp(-b\vec{g} \cdot \mathbf{D}\vec{g}), \tag{2.12}$$

where S_0 is the signal intensity without the gradient pulse, b is the so called b-value, $\vec{g}$ is the gradient pulse vector, $\mathbf{D}$ is the tensor matrix.

2.2.1 Bloch-Torrey Equation and Gradient Pulse

In 1956, Torrey added a diffusion term $+\mathbf{D}\nabla^2\vec{M}$ to the Bloch equations (see Section 2.1.2) [Tor56]:

$$\frac{d\vec{M}}{dt} = \gamma(\vec{M} \times \vec{B}) - \begin{pmatrix} \frac{M_x}{T_2} \\ \frac{M_y}{T_2} \\ \frac{M_z - M_0}{T_1} \end{pmatrix} + \mathbf{D}\nabla^2\vec{M}, \tag{2.13}$$

where ∇^2 denotes the Laplace operator. This spatial differential operator is applied on the vector field $\vec{M}$.

Bloch-Torrey equation (Equation 2.13) states that the change of $\vec{M}$ with respect to time is higher in sample with inhomogeneous magnetic nuclear magnetization. This fact is exploited in an MRI scanner to localize the protons and to measure the apparent water diffusion. A gradient magnetic field B_1, which the strength varies linearly along a specified direction through the scanned volume, causes the Larmor frequency to vary as a function of space. This effect

is used to spatially encode the positions of the nuclei and makes it possible to construct a volumetric image. Furthermore, when the water molecules diffuses in the same direction of the gradient $\vec{B_1}$ the signal emitted by protons is weak, and when the molecules diffuses perpendicularly to to the direction of gradient $\vec{B_1}$ the signal is strong. By performing several measures with different gradient direction, it is possible to compute the diffusion matrix $\mathbf{D}$.

2.3 Diffusion Tensor Imaging

Diffusion Tensor Imaging (DTI) is a method in which Magnetic Resonance Imaging (MRI) scanners are used to measure the water diffusion in the human body. The data obtained from those devices are volumetric images in which each voxel is a diffusion tensor giving information about the local water diffusion. Since the water diffusion is influenced by the body tissue structure, DTI produces images that show the structures such as heart muscle or the brain white matter.

The diffusion tensor matrix $\mathbf{D}$ is estimated from several diffusion weighted images acquired with different gradient directions, that is, solving Equation (2.12) for $\mathbf{D}$ with several values of S,$\vec{g}$ and b.

[BML94]

2.3.1 Fractional Anisotropy

The Fractional Anisotropy is [BP96]:

$$FA = \sqrt{\frac{1}{2}} \frac{\sqrt{(\lambda_1 - \lambda_2)^2 + (\lambda_2 - \lambda_3)^2 + (\lambda_3 - \lambda_1)^2)}}{\sqrt{\lambda_1^2 + \lambda_2^2 + \lambda_3^2}}, \tag{2.14}$$

where λ_1, λ_2 and λ_3 ared the eigen vectors of the diffusion matrix $\mathbf{D}$ (see Section 2.2).

The FA is a scalar metric that describes how anisotropic the diffusion is. This value is high when diffusion ellipsoid tends to a cigar shape (high anisotropy) and low when the ellipsoid tends to a sphere (low anisotropy). Compared to the diffusion matrix $\mathbf{D}$, the FA value contains less information since it discards the specific diffusion directions though it tells about how much oriented the diffusion is.

With the assumption that water molecules diffuse faster along the fibers than perpendicular to them [LBBL$^+$88], a measure of highly anisotropic indicates a highly fibrous tissue. Since the FA is a measure of the anisotropy, an FA image gives information about the location of the fibrous tissue.

2.4 Tractography

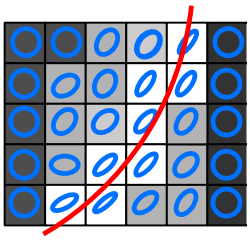

Figure 2.6. By following the main direction of the diffusion tensors (blue ellipsoid) we obtain the path of the fiber tracts (red curve).

Tractography is a technique to visualize fiber tract of fibrous tissue such as muscle or brain white mater. The fiber tracts are visualized as curves in 3D space. In the visualization of brain white matter, this technique shows the connection structure between different part of the brain.

The directionality provided by the tensor images are used to compute curves representing the fiber tracts. Because water molecules diffuse along rather than across the fiber tract due to physical constraint caused by the myelin structure [LBBL+88], the direction of the water diffusion gives us information about the orientation of the tracts. Since DTI images provide water diffusion information at each voxel by mean of diffusion tensor, it is therefore possible to compute the fiber tract paths. In Section 2.2 we have seen that main diffusion direction can be obtained from the diffusion using eigenvector algebra. So a vector field can derived from a DTI image in which each vector represents the main diffusion direction. Assuming that a single vector represents also the local direction of the fiber tracts, we can naturally expect that following the direction of those vectors traces the paths of the fiber tracts (see Figure 2.6).

Tracking algorithms are used to compute fiber tracts from diffusion tensor images. There are mainly two approaches to infer the path of the neural tract from DTI images. Tracking algorithms can be classified into two categories, either local or global [MvZ02]. In the local approach, the path of the tracts are estimated by following the main diffusion direction from voxel to voxel, by mean of streamlines as in fluid flow visualization. The global approach considers all the voxels to find a path between two given voxels in order two minimize an energy function.

Chapter 3

Dealing with occlusion

In this section, we first describe what is occlusion, why it appears and what is the impact on fiber tracts visualization. Then we present the common techniques used to decrease occlusions. Finally, we introduce a novel technique that decreases occlusion, that is, Fiber Tract Bundling (FTB).

3.1 Occlusion

Occlusion generally appears when rendering a three-dimensional scene. Because a scene is often composed of several opaque objects at different locations in space, from a given point of view some object are partially or completely hidden by other objects (see Figure 3.1). This phenomenon appears when performing a realistic rendering. The rendering algorithm, while solving the visibility problem, draws visible objects and discard occluded objects, as it is in a real image (e.g. a picture taken from a camera).

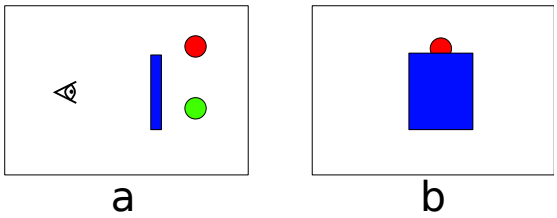

Figure 3.1. (a) Spatial relation between the viewer and three opaque objects: a blue wall, a red sphere and green sphere. (b) From the viewer perspective, the blue wall occludes partially the red sphere and completely occludes the green sphere.

The tracking algorithm generates a large number of three-dimensional curves. The number of generated curves is in the order of hundred thousands. Rendering such a large number of curves on a standard screen produces inevitably occlusion (see Figure 3.2). As a consequence, this way of visualizing three-dimensional curves does not offer insight into the inner structure of the brain, because a large number of curves are occluded by other curves. In Figure 3.2,

the surface of the brain is visible, but because of occlusion, it is impossible to observe how the neural tracts are organized below the surface.

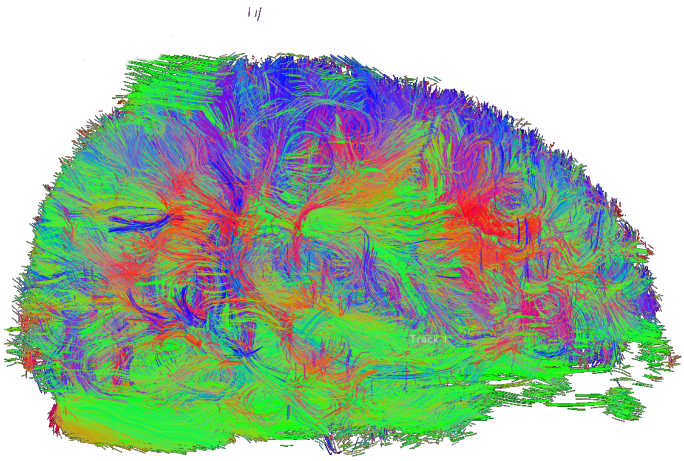

Figure 3.2. Sagital rendering of a large set of neural tracts that creates occlusions.

3.2 Common Methods to Reduce Occlusion

Various simple strategies have been developed to decrease occlusion. The traditional techniques mainly consist of filtering out some curves to decrease their number. The techniques are usually global filtering, length filtering and Region of Interest (ROI) filtering. In the global filtering three-dimensional curves are randomly removed given a filtering ratio. In length filtering, only the curves falling into a given length range are kept. In ROI filtering a three-dimensional object (e.g. a plane or a sphere) is locally placed and only the curves intersecting the ROI object are kept. Those filtering techniques can be combined to obtained a desired visualization.

3.2.1 Global Filtering

The global filtering consists of filtering out a fraction of the total number of tracts randomly. Figure 3.3 shows the results of filtering out 98% of a set of tracts. This filtering give a good overview of the whole brain.

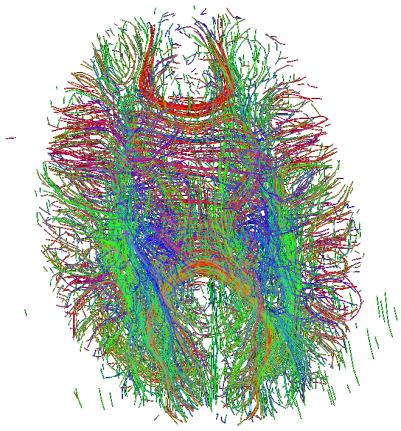

Figure 3.3. 98% of the fiber has been filtered out.

3.2.2 Length Filtering

The length filtering consists of discarding the tracts whose length are not into a range defined by the user. This filtering can be use to remove the very small tracts that can be considered as noise.

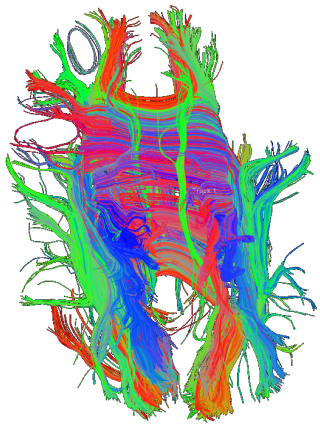

Figure 3.4. Neural tracts whose length are less than 90 mm has been filtered out.

3.2.3 ROI Filtering

ROI filtering consist of defining a region by means of simple geometric objects such as cube, spheres or plane and visualizing only the tracts that intersect the ROI. This technique is useful when we are interested in which tracts pass through a specific location. Further, if the intersecting tracts are long, it is possible to visually follow them and see wich region of the brain they are connecting.

Figure 3.5 and 3.6 show examples of an ROI filtering using a sphere and a place respectively.

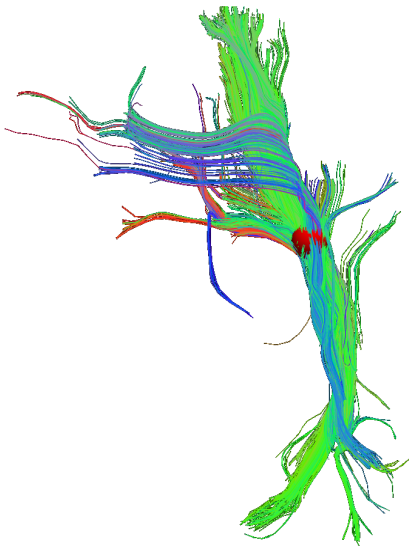

Figure 3.5. Neural tracts passing through the red sphere are kept, the other one are filtered out.

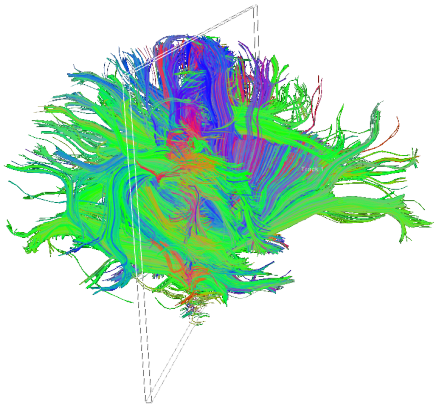

Figure 3.6. Neural tracts passing through the plane are kept, the other one are filtered out.

3.2.4 A novel approach: Fiber Track Bundling

The common techniques presented in here, are very simple and straighforward. The problem with those techniques is that the user must know exactly what he is looking for. Also, those techniques tackle the occlusion problem by discarding tracts without considering the anatomy; there would be some information related to the anatomy that is lost during the filtering of tracts.

Fiber Track Bundling (FTB) aims at decreasing the occlusion by providing an abstracted version of the tracts. The abstraction is computed by considering globally all the tracts. The tracts are bundled based on their similarities. In this way anatomical structures are expected to be visually reavealed automatically. FTB is detailed in Chapter 4.

Chapter 4

Fiber Tract Bundling

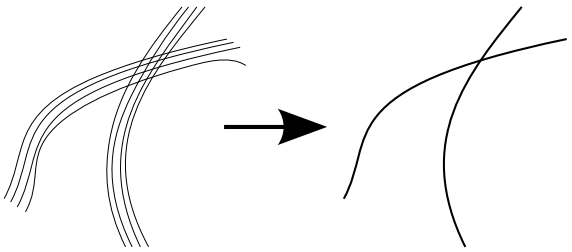

Figure 4.1. The aim of FTB is to provide an abstract representation of a set of curves.

Fiber Track Bundling (FTB) is a technique that produces scalable abstraction of fiber tracts and meanwhile it decreases occlusion [EBRI11]. Figure 4.1 illustrates the aim of FTB. This technique is inspired from a graph visualization technique named Force-Directed Edge Bundling [HvW09]. FTB aims to give insight into the structure of a set of neural tracts obtained from tracking algorithms by offering different scales of simplification.

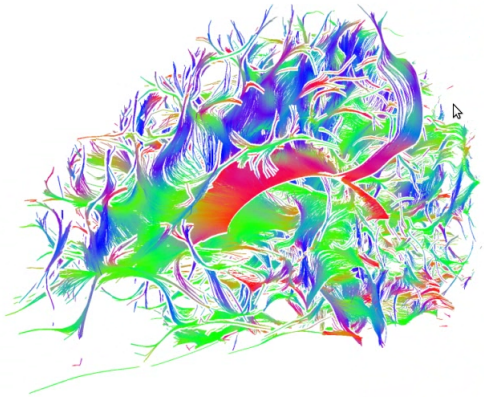

Figure 4.2. Visualization of a bundled tract set revealing at the center the sheet-like structure of the corpus callosum, which is the anatomical structure connecting the two halfs of the brain.

Figure 4.2 shows a set of tracts computed from a DTI image of a head. The color encodes the local direction of the curve. The tracts have been bundled and a sagital cutting plane has been placed offering a cut view of the brain. We can see the corpus collosum in the center of the image as a sheet like structure. This anatomic structure has been simplified by the FTB technique.

FTB achieves the simplified versions of the tracts by modifying the position of their representative curve points so that the curves are grouped together to form bundles. This bundling is obtained by moving similar pairs of points belonging to different tracts toward each other as illustrated in Figure 4.3. The moving of the points causes the tracts they belong to to move. Pairs of points are considered similar when a similarity criteria (i.e. close distance between pair of points, similar local curve unsigned direction) are full filled. The result of the similarity searching can be formally represented as a graph, in which each vertex represents a point and an edge connecting two vertices exists between similar points.

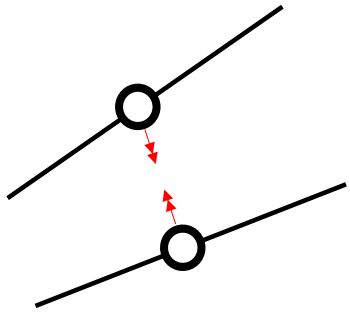

Figure 4.3. FTB achieves bundling by moving similar points towards each other.

The FTB technique is composed of two steps. In a first step the curve points are analyzed in order to find similar points ((see Section 4.1)). In the second step the similar points are moved toward each other in an iterative manner(see Section 4.2).

4.1 Similar Points Searching

The first step of FTB is to search through a fiber data set for the tract segments that shows local similarity. The local similarity is defined from the perspective of the points belonging to the tracts.

Two points $\vec{p}$ and $\vec{q}$ belonging to different tracts are considered similar if they fulfill the following criteria:

- Proximity: the distance between $\vec{p}$ and $\vec{q}$ is smaller than a given length $d_{\max}$.
- Orientation: at least one of the segments incident to $\vec{p}$ is approximately parallel to one of the segments incident ot $\vec{q}$, where "approximately parallel" means that the angle between the segment is smaller than a given angle θ_{par}.

- Nearest neighbour mutuality: the nearest neighbour relation of $\vec{p}$ and $\vec{q}$ is approximately mutual, that is, it holds that $|index(nn(p)) - index(q)| \leq 1$, where the function $index(\vec{v})$ returns the index of $\vec{v}$ on the tract to which it belongs.

The FTB algorithm compares every pairs of points within the data set and tests whether they are similar as defined above. During this phase, a similarity graph G is built in which each vertex represents a point on a tract and an edge connecting two points signifies that these two points are similar.

In the second step (see Section 4.2), G is used to move similar points toward each other.

4.2 Iterative Bundling

The second step of the FTB technique is to move similar tracts points toward each other in order to form bundles. The similary graph computed during the similar point search is used.

One iteration of the algorithm goes as follows. For each pair of points $(\vec{p}, \vec{q})$ in G, $\vec{p}$ and $\vec{q}$ are displaced toward each other so that they meet halfway at $\frac{\vec{p}+\vec{q}}{2}$. Because a point can be similar to several points and therefore may be influenced by several points, its position is not updated directly, rather its displacement is accumulated and later used to update the point position at the end of the iteration. When a vertex is being influenced by several vertices, its displacement vector is divided by the number of incident vertices in the similarity graph.

The algorithm runs typically 40 iterations to achieve a bundled state.

Chapter 5

Research Question: How reliable are the bundled tracts?

We have seen in Section 4 that FTB reduces the occlusion of a dense curve set by creating a scalable visual abstraction.

A main issue occurs with the intrinsic behavior of FTB, that is, this method groups the curves into bundles by changing the position of the vertices representing the curves. The geometry of the curves is therefore distorted resulting into a loss of information about the anatomical location of the bundles. Depending on the application, this loss of information may be significant or not. A neurologist may be only interested whether two distant regions of the brain are connected. For such application the exact location of the fiber bundle is not relevant. However, we can imagine a neuro-surgeon looking at those visual abstraction and wondering how relevant are the bundles in terms of location.

Though FTB does reveal large scale structures such as the corpus callosum that connects the two halfs of the brain, it is not clear whether smaller structures are revealed the same way. When we look at Figure 4.2, we see that the corpus collosum has been revealed and that FTB has simplified this anatomical structure into a sheet-like structure, which is indeed an appropriate abstract representation of the corpus collosum. However the corpus collosum is a major structure in term of size, so we may think that is not possible for the FTB algorithm to "miss" this structure. This leads us to wonder whether the same abstracting phenomenon occurs with smaller anatomical parts, particularly in the region at the surface of the brain where the grey matter is located.

Our research is to evaluate how faithful are the bundled tracts produced by FTB in terms of position and shape.

In order to answer this research question we developed an evaluation method (see Section 6) that enables a user to investigate the behavior of FTB interactively.

Chapter 6

FTB Evaluation Method

FTB modifies the curve point locations. This displacement consequently results in a loss of information related to the anatomy. In order to evaluate this loss of information, we have developed an evaluation tool. We designed this tool with two main objectives:

1. Visualizing the static bundling situation for a given $d_{\max}$.
2. Observing the bundling process behavior with respect to the anatomy.

Also, we want this tool to be interactive so the user can observe the behavior of FTB in an explorative manner.

6.1 Dimensionality reduction

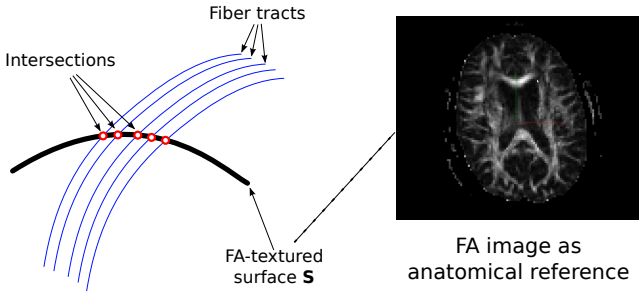

Figure 6.1. The tract are intersected with a surface **S** in order to decrease the dimensionality. The surface **S** is textured with the FA image used as an anatomical reference.

With objective (1), we want this method to consider all the tracts generated by the tracking algorithm and transformed by the FTB algorithm. So we can observe what is happening to all of them. But in this way we are facing a major occlusion problem: it is very difficult or even impossible to visualize such a number of tracks on a computer screen (see Section 3.1).

We solve the occlusion problem by decreasing the problem dimension. We compute the intersection of the tracts with a two-dimensional surface **S** embeded into the three-dimensional space, which has a skull-like shape for this evaluation (see Section 6.2 for more details). The results of the intersection is a set of points that are used as images of the tracts. In this way the dimensionality of the problem is decreased from three to two dimensions, that is, instead of curves we are now visualizing points. When the tracts are bundled, their intersection point with the surface changes accordingly, so visualizing only the intersection points give us an insight about the influence of the FTB algorithm upon the represented tracts while decreasing the occlusion.

The surface **S** can be arbitrary defined and it is used as a Region of Interest (ROI). But obviously it has to passe through the space domain of the tracts, thus the space domain of the DTI image. The user defines **S** as his interest of the locations where he would like to observe the FTB process.

The visualization of the intersection points decreases the visualization problem dimensionality from three dimensions to two dimensions, that is, we are visualizing points instead of curves. This decrease of dimensions allows the user to visualize the bundling process by considering all tracts, though only the tracts intersecting the surface **S** are observable.

6.2 The Skull-like Shaped Surface

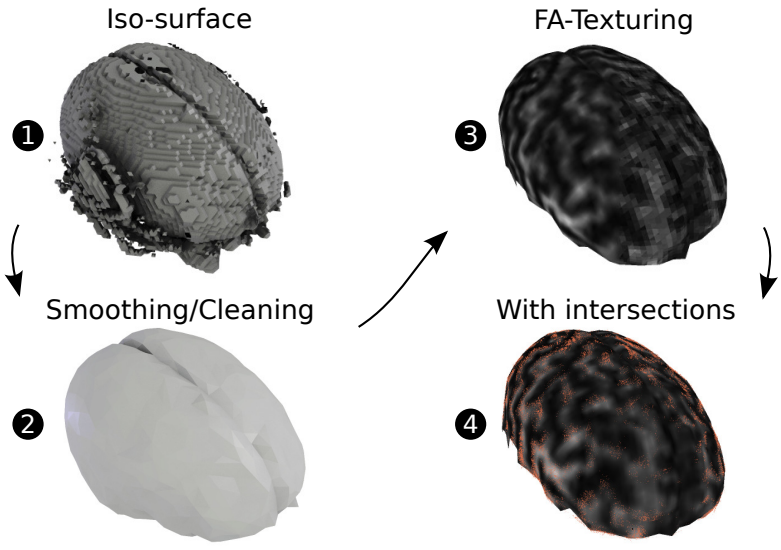

Figure 6.2. Construction and texturing of a skull-like shaped surface **S**. (1) A iso surface extracted from the FA-image. (2) Manually simplified surface. (3) The surface textured with the FA image. (4) The FA-textured surface rendered with the intersecting points.

The surface **S**, which is used to intersect the tracts with to obtain intersection points, can be seen as a Region Of Interest (ROI). It may be defined so that it covers the specific location where we are interested in observing the behavior of the FTB technique.

In this study we are interested in observing the behavior of the FTB algorithm just a bit below the surface of the brain. Becuause, in this area, it is not clear to us whether FTB achieves the same abstraction as it achieves with the corpus collosum. In order to observe the surface of the brain, we first needed to build an appropriate surface to intersect the tracts with.

Figure 6.2 illustrates the construction and usage of the specific surface **S** we are using in this study. First an iso-surface is extracted from the FA-image using the marching cube algorithm, implemented in Mayavi [Ent08], with an iso value that is selected in order to yeld a visually satisfying skull-like shape (Figure 6.2-1). However this iso-surface is not directly usable as it is; it is noisy and it is defined by a large number (76k) of triangles. That noisy surface may generated also noisy intersection points and the large number of triangles defining that surface may slow down dramatically the computation of the intersection with the tracts. Therefore, we need both to decrease the triangle count and to remove the noise by smoothing and simplifying the iso-surface. For these purposes, the raw iso-surface was edited manually using the modelling software Blender [Fou11]. After the editing, the final surface **S** (Figure 6.2-2) is represented by 2k triangles. It is this manually simplified surface that is used to compute the intersecting points with the tracts set. Further, the edited surface **S** is reused during the visualization to provide the user with contextual information and reference to the anatomy. The FA-image is used as an anatomical reference. It is used to texture the surface **S** (Figure 6.2-3). Finally, the intersecting points are rendered slightly above the FA-textured image. The surface **S** textured with the FA-image and the rendering of the intersection points above it allow the user to observe the result of FTB technique with respect to the anatomy (Figure 6.2-4). Additionally, we would like to observe not only the surface of the brain but also how the FTB algorithm behaves deeper to the center of the brain. For this purpose, we used the same skull-like shape but scaled down and displaced at two additional positions as illustrated in Figure 6.3.

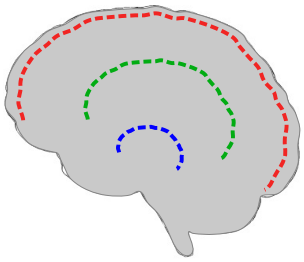

Figure 6.3. The same surface is used at three differents locations and scales; slightly (red), mid-way (green) and deeply (blue) below the brain's surface.

6.3 FA image as anatomical reference

The second objective of the method is to compare the FTB results with the anatomy. This objective is reached by displaying the Fractional Anisotropy (FA) image, which is used as an anatomical reference. We have seen in Section 6.2 that the surface **S** is texture with the FA-image. The rendering of the FA-image nearby the intersections points gives the user useful visual cue about the anatomy and therefore allow the observation of the behavior of the FTB technique with respect to the anatomy.

We used the FA-image as an anatomical reference. We know that the anisotropy of the water diffusion is caused by the interaction of the water molecules with the fibrous material and that the FA value is metric that tells how anisotropic the diffusion is. With some care, we can intrepret a region with a high FA value as region with a high density of parallel fibers and a region with a low FA value as a region containing fewer parallel fibers. In other words, the FA can represent the "fibrousness" of the tissues and gives a good visual reference of the fiber tract locations. We said "with some care" because there are situations in which a voxel containing fibrous tissue is assigned with a low FA value. Those are the voxels in which the contained fibers are oriented in different directions, that is, they are not homogeneous in term of orientation (e.g. crossing fibers). In that case the FA value value would be low compared to voxel containing homogeneously oriented fibers. But for anatomical structures bigger than one voxels the FA value gives confident information about the "fibrousness" of the tissue.

The FA image is used to texture the surface **S**, or more precisely, any point $\vec{p}$ of **S** is colored with a color mapping the FA value at the location of $\vec{p}$. This texture mapping is realized by using the positions of the triangles representing the surface as texture coordinates. The surface **S** textured with the color mapping of the FA value provides the user with information about the anatomy.

6.4 Interaction

The visualization of the intersecting points with the FA-textured surface **S** allows a user to visualize the bundling process and to compare the curve displacement against an anatomical reference.

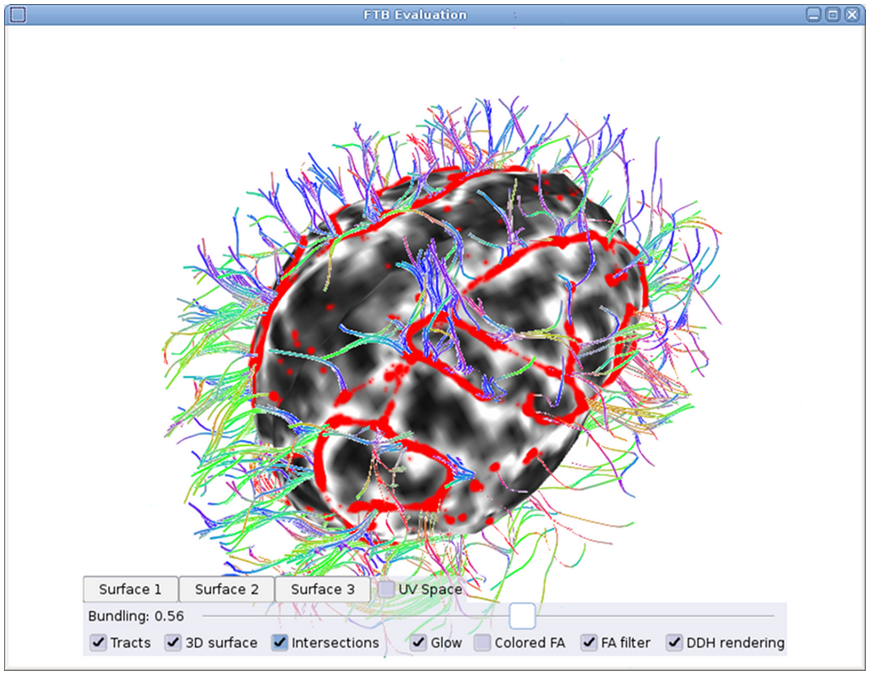

Figure 6.4. Screenshot of the interface of our visualization tool used to evaluate FTB.

Figure 6.4 is a screenshot of the interface of our visualization tool designed and used to evaluate FTB. The surface **S** is rendered with the FA-image as texture such that each point $\vec{p}$ of **S** has a color function of the FA value at the location of $\vec{p}$.

The points being the intersections of the tracts and **S** are rendered in red, with a glow effect wich results into a the cloud look. This cloud rendering gives the user visual information about the density of the points. This cloud rendering is achieved by rendering each point as a transparent disk with varying opacity; the opacity is high at the disk's center and it decays as the distance from the center increases. The disks are blended. This effect results in creating an opaque region where the point density is high and a transparent region where the point density is low.

The user can rotate the view so that he can observe the scene from arbitray angle by dragging the mouse with the left button. There is two type of rotations: orbiting or pivoting. The orbiting rotation makes the view to orbit around the center of the scene, and it is achieves by dragging the mouse in the inner area of the screen whereas the pivoting rotation rotates the view about the viewing

direction, and it is achieves by dragging the mouse in one of the four borders of the screen. Also, the view can be zoomed in and out by using the mouse scroll button or by dragging the mouse up and down with the right mouse button pressed.

The user is provided with an option pannel at the bottom of the screen. The options are organised in three lines. The first line consists of three buttons, which is used to select between the three position of the surface as described in Section 6.2, and a checkbox that toggle the view between the 3D space and UV space. The UV space is the projection of the surface into the 2D plane. The second option line contains a slider that controls the FTB bundling strength. This slider allows the user to interactively change the bundling strenght and visualize the result interactively. The last option line contains seven checkboxes. The first three checkboxes are used to enable or disable the rendering of elements such as the tracts, the surface **S** and the intersection points. When the "Glow" option is enabled, the intersection points are rendered as clouds and when this option is disabled, the points are rendered as flat regular pixels. The "Colored FA" option allows the user to toggle between black and white FA-texture or colored FA-texture (where the color indicates the major main diffusion direction). The "FA filter" controls whether a trilinear filter is applied or not on the FA-texture. And the "DDH" option activates the Depth Dependant Halo [EBRI09] for rendering of the tracts.

6.5 Implementation

6.5.1 Overview

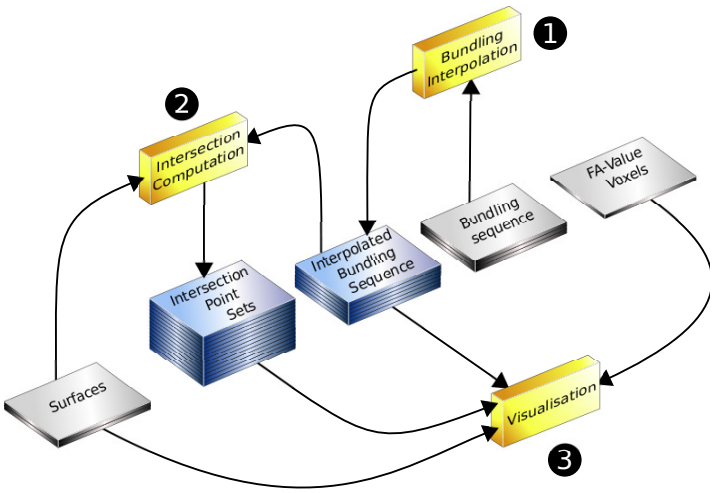

Figure 6.5. Work flow diagram of the evaluation method; Three ordered processes are represented in yellow, given data are in gray and computed data are in blue. The arrows indicate the data flow from sources to destinations.

The aim of the evaluation tool is to provide an interactive visualization of the FTB result with respect to an FA image textured on the surface **S**. Figure 6.5 illustrates the work flow necessary to perform this evaluation.

The first step of the work flow is the bundling interpolation (1), which is needed to obtain smooth transitions while the user is changing the bundling strength. For our study we have 8 sets of tracts resulting from the FTB algorithm. Those 8 sets were computed with a different search radius $d_{\max}$, which started at 0 mm (non-bundled) for the first set and was increased in the following sets. The transition between the sets were very abrupt when visualized. Since we want the user to visualize a smoother transition, we compute linear interpolations of the tract sets. The Section 6.5.2 details the tract sets interpolation. We typically computed 40 interpolated data sets out of the 8 original data sets.

The second step is the intersections computation (2), which consists of computing the intersection points of all the interpolated tracts with the surface **S** represented as a polygonal mesh.

The last step is the visualization (3). This process is fed with the interpolated bundling sequence, the intersections points, the surface **S** and the FA-image. All those data are used to provide the user an interactive vizualisation used to investigate the FTB behavior with respect to the anatomy.

6.5.2 Interpolating the bundled tracts

We were provided with 8 datasets, each containing a bundled tract set obtained from FTB algorithm with different values of $d_{\max}$. All the 8 datasets were computed from the same original tracts sets. The first tract set has a value of $d_{\max} = 0$ mm, that is, the tract set is not bundled. The value of $d_{\max}$ was increased for the next 7 files such that $(d_{\max})_i < (d_{\max})_{i+1}$, where $(d_{\max})_i$ is the search radius used to compute the tract set with index i. We can use those 8 datasets as a bundling sequence of the same tracks set.

We wanted our visual tool to allow the user to smoothly visualize the transitions of the bundling sequence. However, we had only 8 bundling levels and the transition from one level to another were very abrupt. Therefore, we needed to interpolate the 8 files in order to obtain smoother transition between the tract sets.

In order to avoid heavy computation that could decrease the frame rate of the visualization, we compute the interpolated tract sets offline, that is, we compute a desired number of interpolated tracts (We typically computed 40 data sets out of the 8 data sets) and save them on disk as precomputed data prior to the visualization.

An interpolated tract set for a given search radius $d_{\max}$ is computed as follow. First we search the two tracts sets with index i and $i + 1$ that defines the range bounding of $d_{\max}$ such that $(d_{\max})_i < d_{\max} < (d_{\max})_{i+1}$. Once the

bounding indices i and $i+1$ are found, we compute the interpolant t:

$$t = \frac{d_{\max} - (d_{\max})_i}{(d_{\max})_{i+1} - (d_{\max})_i},$$

where $t \in [0, 1]$. Then, the interpolated position for each vertex $\vec{v}$ is given by the linear interpolation :

$$\vec{v} = (1-t)\vec{v}_i + t\vec{v}_{i+1},$$

where $\vec{v}_i$ is the position of vertex $\vec{v}$ in the tract set with index i.

6.5.3 Computing the intersections

A bundling sequence consists of several tract sets ordered by $d_{\max}$. Each set was computed using the FTB algorithm with a different value of $d_{\max}$. Visualizing those sets successively would results into an animation in which a non-bundled tract set is progressively bundled as the bundling strenght increases. The user is able to control the bundling strength interactively.

Changing the bundling strenght results in changing the position of the tracts, and therefore the intersection with the surface **S**. Recomputing the intersections points while the user is changing the bundling strength would cause an overhead that would dramatically decrease the visualization frame rate.

In order to provide the user with a visualization tool that runs at an interactive frame rate, we pre-compute the intersection points and save them on disk. In this way the computation is not performed during the visualization and therefore the visualization process is free from this overhead.

The intersection points are computed for each tract set resulting from the interpolation process and for each surfaces (we typically have 40 interpolated tracts set and the 3 surfaces resulting into the computation of 120 point sets).

The computation of the intersection points of a tracts set T and a surface S represented as a set of triangles is performed as follows. We search for each triangle of S the potentially intersecting tract segments. In order to accelerate this search, we compute an octree covering the surface S. We use an accelerating structure only for the tract set segments and not for the triangles representing the surface **S**, because the number of the tract segments is very large (2.0M) while the number of triangles is low (2k). Using two accelerating structures would be an overhead considering the low number of triangles. By using an octree covering S, the complexity of the searching of tracts segments that potentially intersect a given mesh is:

$$O(t \log(n)),$$

where t is the number of triangles and n is the number of tract segments. One iteration consists of first searching the tract segments that potentially intersect a given triangle. When this search is done, the intersection points of the potential intersecting tracts segments with the given triangle are determined and saved.

Then the iteration considers the next triangle. The iterations stop when all the triangles of S have been processed.

The intersection points for each tract set and each surface S is computed and saved to the disk as a preparation for the visualization.

Our implementation of this algorithm, running on a machine equiped with an Intel(R) Pentium(R) 4 CPU at 3GHz and 1 Go RAM, computes in 12 minutes the intersection points of a sequence of 40 bundled tract sets, each composed of 2M of tract segments, with a surface composed of 1K triangles placed at 3 different positions.

Chapter 7

Results

7.1 Displacement Analysis

FTB creates tract bundles by deforming the tracts locally. This is done by changing the position of the points belonging to the tracts. We are interested in how much the points are displaced from their original position.

In order to perform this analysis, we compute for each point $\vec{v}$ its difference $||\vec{v}_i - \vec{v}_0||$, where $\vec{v}_j$ is a the position of the points $\vec{v}$ with the bundling index j. The result of this computation is aggregated and presented as histograms representing the displacement distribution (see Table 7.1) and as a statistics table (see Table 7.2).

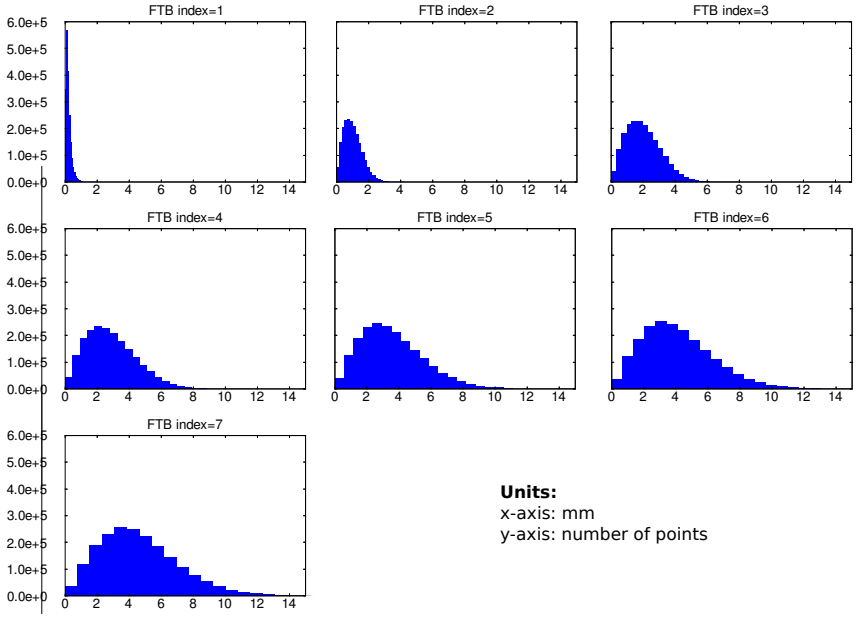

Table 7.1. Vertex displacement distribution per bundled tract sets. The x-axis is the displacement from original position (in mm) and y-axis is the number of vertices.

FTB index	mean (mm)	var (mm)	min(mm)	max (mm)
0	0.0000	0.0000	0.0000	0.0000
1	0.2072	0.0244	0.0000	1.9573
2	1.0082	0.3088	0.0000	4.2964
3	2.0089	1.1120	0.0000	8.0925
4	2.8551	2.3487	0.0000	11.6030
5	3.5489	3.6143	0.0000	14.6157
6	4.1193	4.6829	0.0000	17.1593
7	4.5832	5.6305	0.0000	19.2375

Table 7.2. Displacement statistics for 7 bundled tract sets indexed from 0 (non bundled) to 7 (highly bundled).

We observe that the displacement distribution follows a skew distribution. The mean of the distribution increases as the bundled index increases, and so for the variance.

The increase of the displacement with the bundling index is coherent with the FTB algorithm. Since a larger index corresponds to a larger $d_{\max}$, this means that the points will be influenced by farther neighbor points and thus the point displacements will be larger.

This analysis tells us how faithful FTB is in term of position. That is by observing a bundled tract for a given $d_{\max}$, we know that the original fibers are located nearby the bundled tract with a probability given by its displacement distribution. For example, with a bundled tracts at bundling index 3, we know that the original fibers are not farther than 9 mm.

7.2 Behavior w.r.t. FA image

We use a three-dimensional surface representing the surface of the brain, roughly located within the space between the skull bone and the brain. This surface is used at three different positions/scale: (1) slightly, (2) mediumly and (3) deeply below the brain surface.

From a visual inspection, we conclude that FBT is anatomically consistent with 30% of bundling. At this bundling scale we have a more abstract image of the fiber tracts structure while the tracts are still located at the high FA-values. When the bundling scale goes above 30% the fiber tracts become less and less aligned with the FA-image, meaning that the fiber tract are no more anatomically consistent.

From this we conclude that FTB offers a good abstraction of the fiber tract structure, when the bundling strength is carefully controlled.

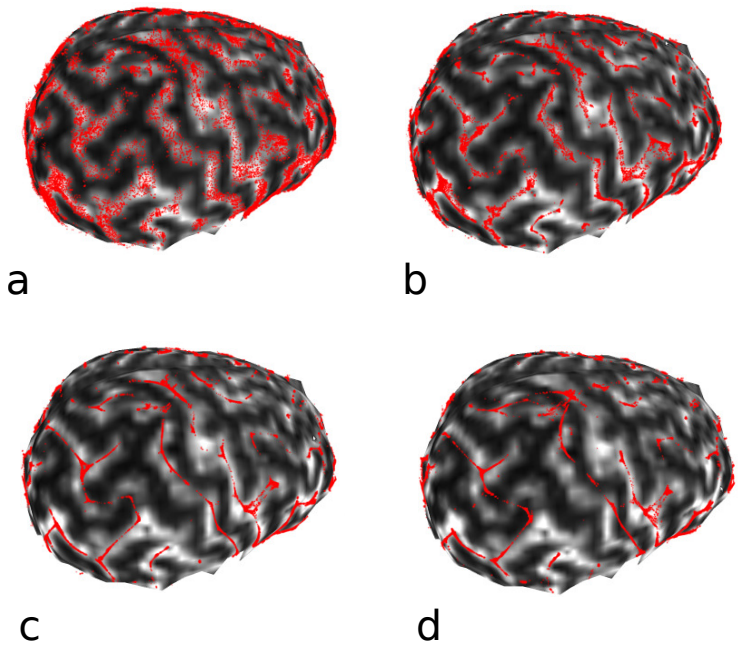

Figure 7.1. FTB scaling.

Chapter 8

Conclusion

In this master project, we have evaluated the Fiber Tract Bundling (FTB) technique by considering how faithful the bundled tracts are in terms of location and shape. In order to perform this evaluation we developed a tool to visually and interactively investigate the behavior of the FTB algorithm with respect to the anatomy. The FA image was used as an anatomical reference since it give information about the location of the fiber tracts. Through a visual inspection using our interactive visualization tool, we found out that FTB gives an abstraction that is coherent with the anatomy when the bundling strenght is approximately at $\frac{1}{3}$ of its maximum.

Bibliography

[Blo46] F. Bloch. Nuclear induction. *Phys. Rev.*, 70(7-8):460–474, Oct 1946.

[BML94] P. J Basser, J. Mattiello, and D. LeBihan. Mr diffusion tensor spectroscopy and imaging. *Biophysical Journal*, 66:259–267, 1994.

[BP96] P. J. Basser and C. Pierpaoli. Microstructural and physiological features of tissues elucidated by quantitative-diffusion-tensor mri. *Journal of Magnetic Resonance*, 111(3):209–219, June 1996.

[BPP48] N. Bloembergen, E. M. Purcell, and R. V. Pound. Relaxation effects in nuclear magnetic resonance absorption. *Physical Review*, 73:679–712, 1948.

[Dam71] R. Damadian. Tumor detection by nuclear magnetic resonance. *Science*, 171(976):1151–3, 1971.

[EBRI09] Maarten H. Everts, Henk Bekker, Jos B. T. M. Roerdink, and Tobias Isenberg. Depth-dependent halos: Illustrative rendering of dense line data. *IEEE Transactions on Visualization and Computer Graphics*, 15(6):1299–1306, 2009. Best Paper Award at IEEE Visualization 2009.

[EBRI11] H. Maarten Everts, Henk Bekker, Jos B. T. M. Roerdink, and Tobias Isenberg. Fiber tract bundling. *Unknown*, 0, 2011.

[Ent08] Enthought. Mayavi. *http://code.enthought.com/projects/mayavi/*, 2008.

[Fou11] Blender Foundation. Blender. *http://www.blender.org*, 2011.

[Gol07] Steven Goldberg. Mris and the perception of risk. *American Journal of Law & Medicine*, 33:229–237, 2007.

[HvW09] Danny Holten and Jarke J. van Wijk. Force-directed edge bundling for graph visualization. *Proceedings of EuroVis*, pages 983–990, 2009.

[LBBL+88] D. Le Bihan, E. Breton, D. Lallemand, Ml Aubin, J. Vignaud, and M. Laval-Jeantet. Separation of diffusion and perfusion in intravoxel incoherent motion mr imaging. *Radiology*, 168(2):497–505, aug 1988.

[LBTMP91] D. Le Bihan, R. Turner, C. T. W. Moonen, and J Pekar. Imaging of diffusion and microcirculation with gradient sensitization: Design, strategy, and significance. *JMRI*, 1(1):7–28, 1991.

[MvZ02] Susumu Mori and Peter C M van Zijl. Fiber tracking: principles and strategies - a technical review. *NMR Biomed*, 15(7-8):468–80, 2002.

[RZMK38] I. I. Rabi, J. R. Zacharias, S. Millman, and P. Kusch. A new method of measuring nuclear magnetic moment. *Phys. Rev.*, 53(4):318, Feb 1938.

[SZZS01] S. Steinhoff, M. Zaisev, K. Zilles, and N.J. Shah. Fast t1 mapping with volume coverage. *Magnetic Resonance in Medecine*, 46(1):131–140, 2001.

[Tan79] J.E. Taner. Sefl diffusion of water in frog musle. *Biophysical Journal*, 28(1):107–116, 1979.

[Tor56] H. C. Torrey. Bloch equations with diffusion terms. *Phys. Rev.*, 104(3):563–565, Nov 1956.